PAPER

Check for updates

Self-biased visible-NIR photodetection enabled *via* a dual-heterojunction n-MoS₂/p-CuO/n-Si design

Tabark A. Fayad,[a] Mohamed Hassan Eisa,[b] Ethar Yahya Salih [iD] *[a] and Asmiet Ramizy[c]

In this study, a comprehensive dual-junction (n-MoS₂/p-CuO/Si and p-CuO/n-Si) evaluation of a self-biased heterostructure was conducted for photodetector applications. Owing to the integration of both junctions, the proposed design offered dual-response functionality, under zero bias, corresponding to the visible (625 nm) and NIR (720 and 808 nm) regions. At zero applied bias, the n-MoS₂/p-CuO/Si heterojunction exhibited a responsivity (R_λ) of 21.04/30.50 mA W⁻¹ and a detectivity (D^*) of 1.0 × 10¹⁴/1.5 × 10¹⁴ Jones at incident wavelengths of 625/720 nm; this highlights the self-biased nature of the fabricated design. The attained values were found to be dramatically increased under a 3 V bias, with R_2 values of 0.144 and 0.124 A/W for the n-MoS₂/p-CuO/Si and p-CuO/n-Si heterostructures, respectively. The observed figures-of-merit consistently reduced as the incident light intensity increased, indicating a strong negative correlation, which was further confirmed by the R^2 value approaching unity (R^2 = 1). The time-resolved features confirmed response/recovery times of 0.27/0.36 and 0.41/0.48 s, respectively, for the addressed heterostructures, highlighting the suitability of this design for efficient, bias-free photodetection over Vis-NIR wavelengths.

1. Introduction

Photodetector-based optoelectronics, specifically those fabricated using Si technology, are being broadly considered for optical and electronic applications, UV/Vis/IR optical communication, flame detection, environmental and biological sensing, and imaging because of their CMOS technology compatibility, easy fabrication process, and low cost.[1–3] Nevertheless, the characteristic restrictions of Si technology, such as constrained absorption in the Vis-NIR range and indirect optical bandgap, have prompted the incorporation of complementary semiconductor metal oxides to boost the spectral response and subsequently the device performance.[4–6] Thus, heterojunction-based Si optoelectronics, dual-band photodetectors in particular, are being further investigated among research and industrial societies due to their benefits compared with their homojunction counterparts; these include high photoresponsive performance, almost zero power consumption, and wide spectral response. Further, dual-band photodetectors have demonstrated excellent potential in this regard, allowing enhanced charge separation effectiveness through wide spectral absorption at zero applied bias. Accordingly, various dual-band optoelectronics have been developed with relatively high photo-responsive properties, including high R_λ, excellent D^*, fast rise/fall times, and high on/off ratio; these include CuO-TiO₂/Si, CuO/Cu₂O/Si, ZnO/ZnTe/Si, and WSe₂/WS₂/p-Si.[7–10] Notably, the combination of p-type CuO, a narrow optical bandgap metal oxide semiconductor with relatively robust absorption within the visible spectrum, along with an Si wafer, has been broadly evaluated. CuO, with p-type conductivity, is known to be favorable for its band alignment with Si, enabling well-organized carrier separation and transport across the formed heterojunction, thereby allowing an enhanced photo-response behavior even under low applied bias.[11–13] Moreover, the integration of a two-dimensional (2D) layered material, like MoS₂, could alter the photodetector functionality. MoS₂ exhibits solid light–matter interaction, excellent scalability, and relatively high carrier mobility;[14–16] when n-MoS₂ is configured onto a p-CuO/n-Si stack, the proposed candidate can facilitate a dual-heterostructure design, enabling spectral lengthening to the NIR range, effective carrier collection, and self-driven operation *via* a built-in electric field. In this context, we report a multi-band (p-n and n-p) dual-junction optoelectronic design. Moreover, a methodical fabrication procedure for the intended dual-band, fast-response, self-driven heterostructure is elucidated. In detail, the proposed heterojunction (n-MoS₂/p-CuO) resulted in pronounced figure-of-merit profiles along a broad range at zero applied bias voltage.

[a] College of Energy and Environmental Sciences, Al-Karkh University of Science, Baghdad, 10081, Iraq. E-mail: ethar988@gmail.com, ethar@kus.edu.iq

[b] Department of Physics, College of Science, Imam Mohammad Ibn Saud Islamic University (IMSIU), Riyadh, 13318, Saudi Arabia

[c] College of Science, University of Anbar, Anbar, Iraq

2. Experimental procedure

The intended dual-heterostructured device (n-MoS$_2$/p-CuO/n-Si) was fabricated *via* a pulsed laser deposition (PLD) process along with selective masking in order to attain a spatially patterned design. In detail, a commercially presented n-type Si wafer (Sigma Aldrich, 100, 1–10 Ω cm) was utilized as the main substrate. The Si wafer was thoroughly cleaned using the RCA standard procedure to remove the undesired contaminants; then, the wafer was diluted with HF to eliminate native oxides. To create the spatially patterned dual-heterojunction foundation (Fig. 1a), the wafer was partially covered, allowing two-thirds to be exposed to the generated plasma plume. Herein, a high-purity Cu target was irradiated at 6 J cm^{-2} using a 2nd harmonic Q-switched Nd:YAG laser (532 nm) with a repetition rate of 10 Hz. The temperature of the Si wafer was maintained at 200 $^\circ$C in an oxygen environment of 10^{-3} mbar, allowing the deposition of a CuO layer; the attained substrate was then allowed to cool naturally to room temperature. Thereafter, two-thirds of the attained geometry was covered, allowing the deposition of MoS$_2$ on one half of the CuO layer (Fig. 1a). In detail, the MoS$_2$ target was ablated by the same laser source (6.5 J cm^{-2}) to obtain the n-MoS$_2$/p-CuO/n-Si heterostructure; the MoS$_2$ film covered one half of the deposited CuO film, as demonstrated in Fig. 1a, forming distinct dual-heterojunctions. In order to enhance the interfacial quality and crystallinity of the deposited layers, the attained geometry was thermally treated in air at 250 $^\circ$C for 45 minutes. Finally, Ag electrodes were deposited by thermal evaporation to define the active device area and ensure reliable electrical contact within the dual-heterojunction architecture.

The structural investigation was conducted using X-ray diffraction techniques (Bruker, AXSD8, XRD), while the optical investigation was performed *via* UV-Vis spectrophotometry (UV-3600, Shimadzu). The topographies of the deposited layers were examined using field-emission scanning electron microscopy (SU8030, Hitachi, FE-SEM). Simultaneously, a room-temperature photoresponsive evaluation was conducted utilizing a source measure unit (Keithley 2400, SMU) in conjunction with a narrow optical-bandpass filter/s (ThorLabs), allowing a wavelength scan from 405 nm to 808 nm. The incident light intensity, transmitted through the filter, was measured at the light incident spot with an LX2-illuminance meter (Japan, Sanwa). Moreover, the time-dependent features were projected by considering 10% to 90% of the entire attained photocurrent (I_{ph}) by histogram search, while the incident light pulse-width was fixed at $\sim$12.5 s.

3. Results and discussion

Fig. 1b depicts the XRD diffraction patterns of the deposited CuO and MoS$_2$ layers, in which the addressed layers showed polycrystalline orientation. Specifically, the XRD spectrum of CuO exhibits five distinct diffraction planes (110), (101), (111), (−202), and (020), which are characteristic of the monoclinic CuO structure, in agreement with JCPDs card no. 80-1919; these planes were identified at 2θ values of 32.426°, 35.407°, 38.641°, 48.684°, and 58.221°, respectively. Simultaneously,
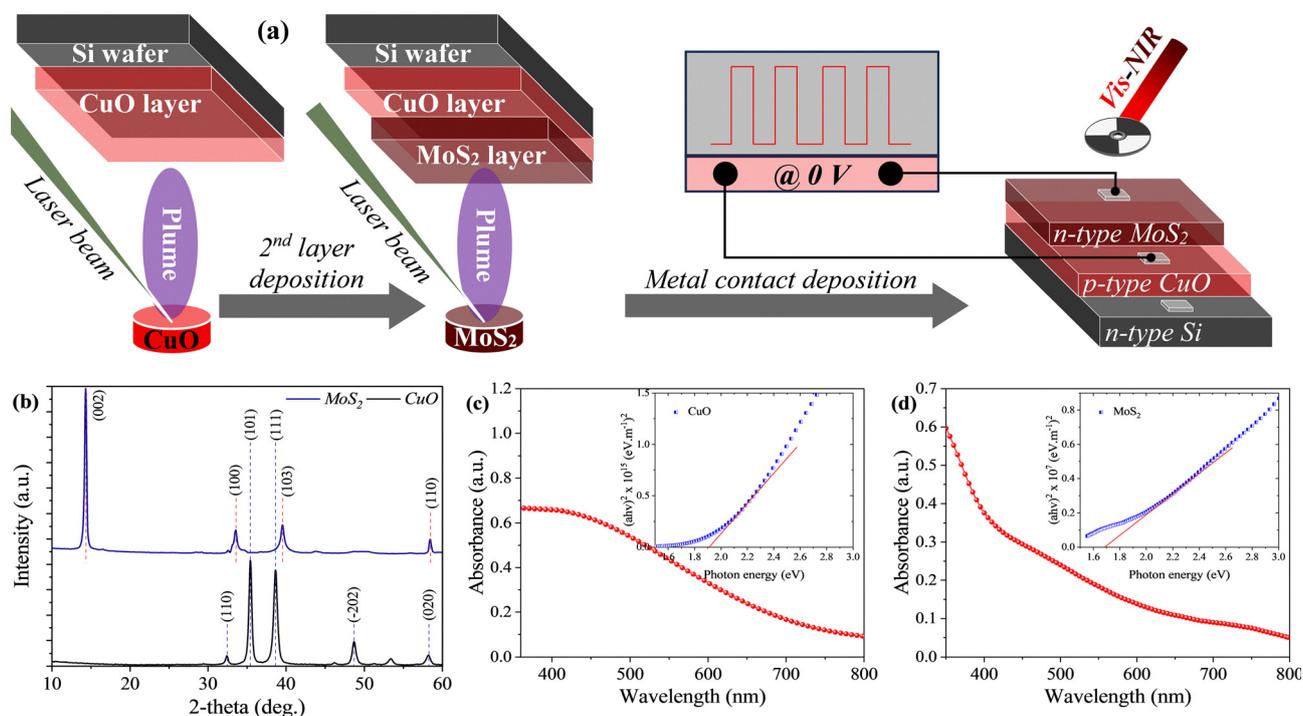

Fig. 1 (a) Schematic of the pulsed laser deposition process for the design of the fabricated device and the measurement set-up. (b) XRD patterns and UV-Vis spectra and optical bandgap (inset) of the deposited (c) CuO and (d) MoS$_2$ layers.

four prominent distinct XRD patterns for the MoS_2 layer were observed at around $2\theta \approx 14.194°$, $33.536°$, $39.542°$, and $58.440°$, which correspond to the (002), (100), (103), and (110) planes, respectively. The positions and sharpness of these reflections indicate well-aligned, high crystallinity structures that closely match the hexagonal $2H\text{-}MoS_2$ phase, as confirmed by JCPDS card no. 37-1492. Optical analysis of the deposited CuO film (Fig. 1c) revealed a broad absorption curve along the visible range, which indicates good light-harvesting ability in the visible spectrum. The optical bandgap of the addressed layer (CuO), estimated according to the Tauc relation,[17,18] exhibited a value of 1.91 eV (see the inset of Fig. 1c). Similarly, MoS_2 (Fig. 1d) demonstrated a smooth increase in absorption from the visible to the UV region; however, the absorption curve lacks an excitonic peak characteristically detected in monolayer MoS_2, which, in turn, suggests bulk-like/multilayer structure formation during the deposition using the PLD method. The optical bandgap (see the inset of Fig. 1d) was found to be 1.68 eV, corresponding to an incident wavelength of $\sim$738 nm. The topography analysis of the CuO layer (Fig. 2a) revealed the formation of relatively compressed and uniformly distributed granular particles, suggesting a polycrystalline structure along random crystallite orientations within the >50 μm scanned area. The particle distribution appears moderately heterogeneous, with isolated bright regions across the scanned area, which could be due to surface roughness and/or localized agglomeration. Such morphological singularities are frequently obtained in CuO films attained using the PLD technique.[19,20] In comparison to the CuO morphology, MoS_2 (Fig. 2b) exhibited a slightly more homogeneous distribution of grain-like features and a smoother surface. The reduction in the bright agglomerate phenomenon indicates a reduced surface roughness and higher film continuity. Such morphology is usual for layered MoS_2, where the interactions of van der Waals (vdW) forces allow compact growth and planar stacking.[21]

The current–voltage (I–V) characteristics of the proposed dual-heterojunction (n-MoS_2/p-CuO/Si and p-CuO/n-Si) under both dark and light settings are shown in Fig. 3a. An unsymmetrical nonlinear diode-like conduct is observed with a clear rectification profile under both dark and illuminated states with respect to the utilized wavelength. In detail, the heightened carriers' diffusion and their recombination with injected charge result in dark current suppression. As the applied bias increases, the diffusion current dominates, leading to a significant dark current growth; in this case, the depletion region becomes thinner while the built-in electric field is nearly debilitated, which, in turn, allows diffusion current domination. The rectification ratios were found to be 10.06 and 7.83, respectively, at 5 V under dark conditions for the named heterojunctions; the attained variation in the rectification ratio could be because of the alteration in carrier recombination as well as defect states at different interfaces. Such interface quality enhancement, in the case of n-MoS_2/p-CuO/Si, may result in higher carrier transport phenomenon and subsequently higher rectifying singularity.[22] It is worth pointing out that similar behavior was noted at different incident wavelengths with respect to the considered heterojunction. Further, the ideality factor (n) was estimated in accordance with Cheung's model, considering a semi-linear plot of the forward dark current[23] (see inset of Fig. 3a). The proposed heterojunctions exhibited n values of 1.7 and 2.1 for n-MoS_2/p-CuO/Si and p-CuO/n-Si, respectively. Such a deviation from $n = 1$ suggests the presence of interface recombination and/or trap-assisted tunneling effects. Fig. 3b and c show the wavelength-dependent photoresponse of the proposed junctions as a function of time-resolved profiles under a 3 V applied bias. Owing to the narrow bandgap of the utilized active layers (CuO and MoS_2), the fabricated heterojunctions exhibited rather broad responsive detection capability. However, two dominant wavelengths (625 and 720 nm) were identified for the n-MoS_2/p-CuO/Si and p-CuO/n-Si heterojunctions, respectively, corresponding to efficient photoinduced carrier generation under the specific incident wavelengths, the absorption edge of the active layers as pre-demonstrated in Fig. 1(c) and (d); this in turn validates the dual function nature of the proposed design. The distinguished photoresponse at 808 nm, in the case of p-CuO/n-Si heterojunction, is mainly due to the window effect of the utilized Si wafer.[24] Such wavelength-dependent behavior could
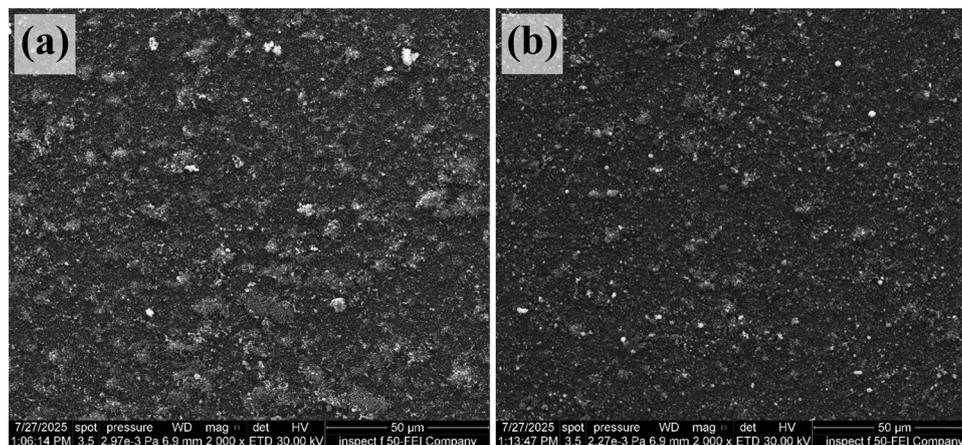

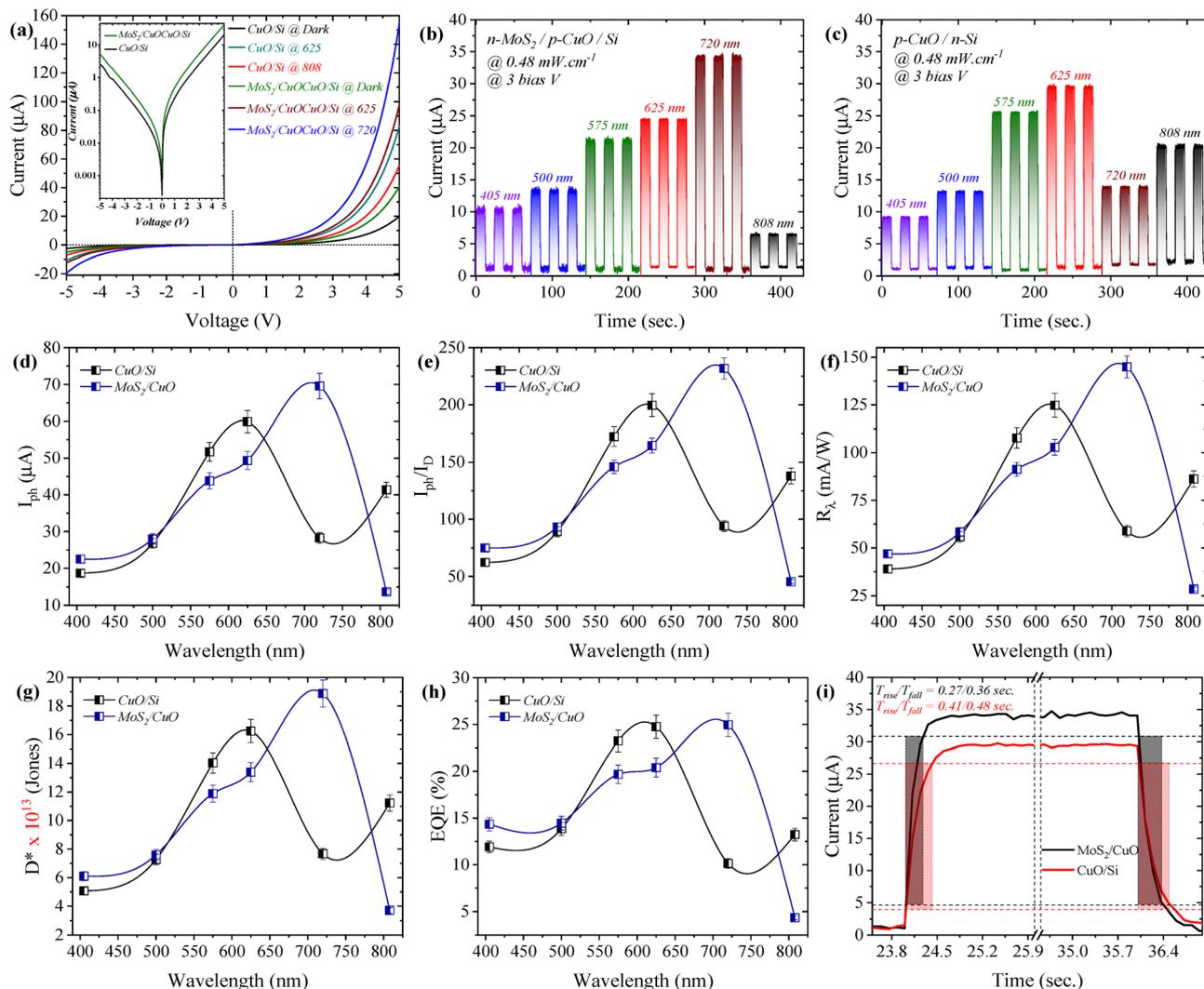Fig. 2 FE–SEM images of the deposited (a) CuO and (b) MoS_2 layers; scale bar of 50 μm.

Fig. 3 Photo-responsive analysis of the fabricated n-MoS$_2$/p-CuO/Si and p-CuO/n-Si photodetectors at a 3 V bias: (a) I–V characteristics, with the inset of semi-log dark I–V, (b) time-based profile of n-MoS$_2$/p-CuO/Si, (c) time-based profile of p-CuO/n-Si, (d) I_{ph}, (e) I_{ph}/I_D, (f) R_λ, (g) D^*, (h) EQE, and (i) response/recovery time of CuO/Si and MoS$_2$/CuO.

be clearly indicated from the I_{ph} profile (Fig. 3c). Four critical figures-of-merit are demonstrated in Fig. 4e–h: light-to-dark ratio $[I_{ph}/I_D]$, responsivity $[R_\lambda = I_{ph} - I_D/P_{in}]$, detectivity $[D^* = R_\lambda A^{1/2}/(2eI_D)^{1/2}]$, and external quantum efficiency $[EQE = (I_{ph}/e)(P_{in}/h\nu)]$.[25,26] Specifically, R_λ (Fig. 3f) demonstrated values of 0.144 and 0.124 A W^{-1} at 720 and 625 nm for n-MoS$_2$/p-CuO/Si and p-CuO/n-Si, respectively, while D^* values of 1.9 × 10^{14} and 1.6 × 10^{14} Jones (Fig. 3g) and EQE of 25 and 24.7 (Fig. 3h) were obtained at the same addressed parameters, respectively. The proposed geometries exhibited response/recovery times (Fig. 3i) of 0.27/0.36 and 0.41/0.48 s, respectively, indicating faster responses compared to the recovery; these were considered under incident wavelengths of 720 and 625 nm, respectively. This, in turn, strongly indicates a faster generation phenomenon compared to recombination.[27,28] The attained sub-second rise/fall time, in both junctions, could be attributed to the interfacial dynamics as well as carrier trapping/de-trapping within the proposed dual-heterojunction. In detail, both PLD-based CuO and MoS$_2$ layers

are polycrystalline (Fig. 1b) along defect states and grain boundaries, which, in turn, causes a localized carrier phenomenon along with prolonged lifetime. Additionally, such structural imperfections might also induce defects/traps, which directly influence the response speed.[29,30] Results evidently suggest that the performance of n-MoS$_2$/p-CuO/Si outweighs that of p-CuO/n-Si due to the ability of the n-MoS$_2$/p-CuO heterojunction in reducing the defect states and/or carrier recombination.

The light intensity-dependent responses of the proposed junctions at the optimum wavelengths and 3 V applied bias are presented in Fig. 4a and b; this investigation was conducted in terms of the time-resolved characteristics. The considered junctions responded linearly to the light-intensity increment, with an R^2 value close to unity ($R^2 \approx 1$). A more detailed examination was conducted into this behavior, considering the I_{ph}/I_D ratio (Fig. 4c), where the considered heterojunction demonstrated linear correlation to the utilized intensity at different wavelengths, suggesting a dynamic role of the active layers.
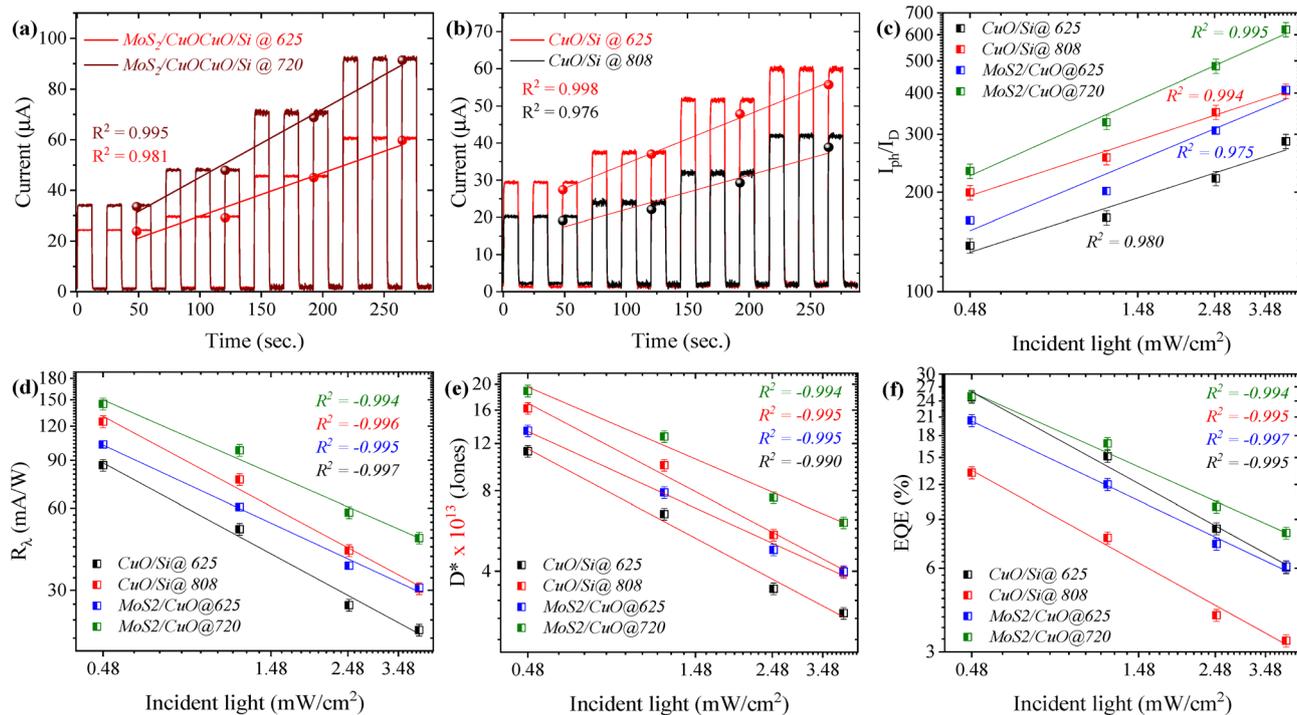
Fig. 4 Intensity-dependent profile: time characteristics of (a) n-MoS$_2$/p-CuO/Si, (b) p-CuO/n-Si. (c) I_{ph}/I_D, (d) R_λ, (e) D^*, and (f) EQE values achieved at a 3 V applied bias.

Other figures-of-merit, including R_λ, D^*, and EQE, exhibited clear inverse trends, as shown in Fig. 4d–f. These characteristics tend to saturate as the incident intensity increases; in detail, R_λ decreased from 0.144 to 0.047 A W^{-1} as the light intensity, for n-MoS$_2$/p-CuO/Si at a wavelength of 720 nm, increased from 0.48 to

4 mW cm^{-2}. Such an occurrence is mainly because the relationship between R_λ and P_{in} is inversely proportional ($R_\lambda \propto P_{in}^{-1}$),[31] while D^* and EQE are mathematically dependent on R_λ. Irrespective of the incident wavelength, n-MoS$_2$/p-CuO/Si demonstrated higher figures-of-merit than p-CuO/n-Si.
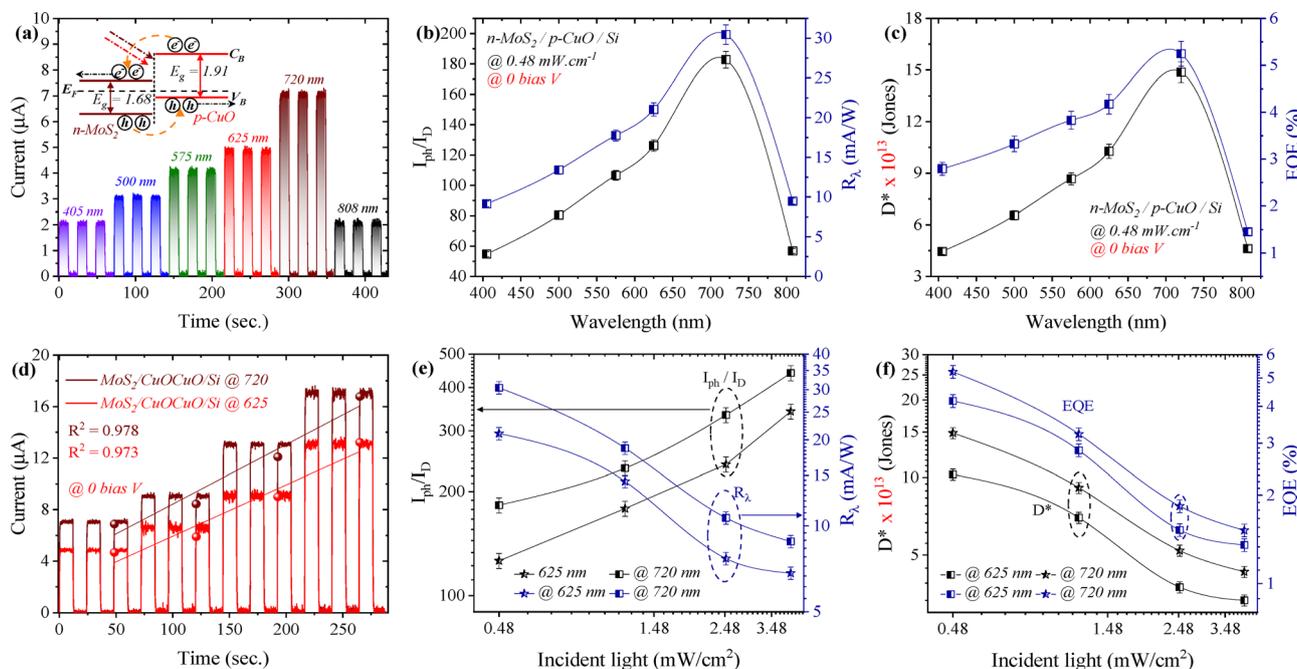

Fig. 5 Self-biased Vis-NIR configuration. Wavelength-based profiles: (a) time-resolved characteristics, (b) I_{ph}/I_D and R_λ, (c) D^* and EQE. Intensity-based profiles: (d) time-resolved characteristics, (e) I_{ph}/I_D and R_λ, and (f) D^* and EQE.

The responsive characteristics, under zero-bias configuration, of the investigated n-MoS$_2$/p-CuO/Si heterojunction were investigated systematically at 0.48 mW cm^{-2} (Fig. 5). Within this particular configuration, the n-Si wafer is left electrically floated; this condition results in the emergence of a photogating phenomenon at the n-MoS$_2$/p-CuO/Si heterostructure's bottom interface. The detected effect not only induces a noticeable photovoltaic response within the proposed heterostructure by facilitating the separation of photogenerated carriers, where zero bias is applied, but also leads to a distinguished augmentation in photoconductive gain.[7] The time-based light response, at zero applied bias, could be explained *via* the band alignment (see the inset of Fig. 5a). In detail, charge transport and carrier dynamics in the n-MoS$_2$/p-CuO/Si heterojunction are governed by specific aspects, including defect concentration, interface state, and band alignment. Particularly, light-induced electron excitation results in so-called band-bending, which, in turn, increases the built-in electric field and subsequently smooths the photogenerated carriers' separation and collection. Incident light induces additional band-bending (see the inset of Fig. 5a), thereby enhancing the electron–hole separation and strengthening the internal electric field, which, in turn, allows more efficient carrier extraction. Therefore, the attained band alignment suppresses the electron–hole recombination and increases the carrier collection efficiency at zero applied bias.

The light-response characteristics exhibited a well-oriented wavelength-dependent profile, indicating the good performance of the proposed heterostructure in the self-driven mode (Fig. 5a), with a considerably low dark current of 90 nA; the fluctuation in the measured dark current mainly resulted from the resolution limitation of our setup. The self-driven feature was further inspected in terms of the related figures-of-merit. The demonstrated figures-of-merit (Fig. 5b and c) delivered a considerable R_λ of 30.50 mA W^{-1}, D^* of 1.5×10^{14} Jones, and EQE of 5.25 at zero applied bias, indicating the self-driven nature of the proposed geometry. In terms of light intensity dependence, the n-MoS$_2$/p-CuO/Si heterojunction was also investigated at zero applied bias under illumination at the optimum wavelengths (625 and 720 nm); the light response (Fig. 5d) demonstrated a linear increase, which indicates the superior light sensitivity of the proposed junction. The I_{ph}/I_D showed a linear increase as a function of light intensity increment (Fig. 5e, black curves). Other figures-of-merit showed a linear decrease as a function of incident light intensity increase (Fig. 5e and f).

4. Conclusion

A self-driven optoelectronic dual-heterojunction (n-MoS$_2$/p-CuO/n-Si) was effectively fabricated through consecutive PLD techniques, integrating spatially decorated films. The photodetector exhibited a multi-spectrum response, under zero biasing, at wavelengths of 625, 720 and 808 nm, crossing both Vis and NIR regions. At 0 V bias, the fabricated n-MoS$_2$/p-CuO/ n-Si heterostructure exhibits R_λ of 21.04/30.50 mA W^{-1} and D^* of 1.0×10^{14}/1.5×10^{14} Jones at incident wavelengths of 625/ 720 nm, confirming the self-driven feature. Such metrics were enhanced at an applied bias of 3 V, with R_λ values of 0.144 and 0.124 A W^{-1} for n-MoS$_2$/p-CuO/Si and p-CuO/n-Si, respectively, attributed to lower interface recombination and improved carrier separation. Additionally, time-resolved features revealed rise/fall times of 0.27/0.36 and 0.41/0.48 s, respectively, for the addressed heterojunctions.

Conflicts of interest

There are no conflicts to declare.

Data availability

All data used are presented in the manuscript.

Acknowledgements

References

1 C. Liu, *et al.*, Silicon/2D-material photodetectors: from near-infrared to mid-infrared, *Light: Sci. Appl.*, 2021, **10**(1), 123.

2 X.-X. Wang, *et al.*, Photodetectors integrating waveguides and semiconductor materials, *Nanoscale*, 2024, **16**(11), 5504–5520.

3 E. Y. Salih, Opto-electrical evaluation of visible blind fast-response nanostructured SnO 2/Si photodetector, *RSC Adv.*, 2024, **14**(38), 27733–27740.

4 S. Jiang, *et al.*, Solution-processed NiO/Si heterojunctions for efficient self-powered UV–Vis-NIR broadband photodetection, *ACS Appl. Electron. Mater.*, 2024, **6**(4), 2525–2533.

5 M. K. Mohammed, *et al.*, Facile synthesis of chitosan-MoS$_2$ over reduced graphene oxide to improve photocatalytic degradation of methylene blue, *J. Sol-Gel Sci. Technol.*, 2024, 1–11.

6 Y. Xu, *et al.*, High-performance CuS/n-Si heterojunction photodetectors prepared by e-beam evaporation of Cu films as precursor layers, *J. Alloys Compd.*, 2021, **884**, 161121.

7 Z. Huang, *et al.*, Integration of photovoltaic and photogating effects in a WSe 2/WS 2/p-Si dual junction photodetector featuring high-sensitivity and fast-response, *Nanoscale Adv.*, 2023, **5**(3), 675–684.

8 S. K. Kajli, D. Ray and S. C. Roy, Efficient UV–visible photodetector based on single CuO/Cu$_2$O core-shell nanowire, *J. Alloys Compd.*, 2022, **895**, 162546.

9 C. Ghosh, *et al.*, CuO–TiO$_2$ based self-powered broad band photodetector. Nano, *Mater. Sci.*, 2024, **6**(3), 345–354.

10 E. Y. Salih, *et al.*, Fast-response self-powered double-heterojunction n-ZnO/p-ZnTe/n-Si photodetector, *Nanoscale Adv.*, 2025, DOI: 10.1039/D5NA00331H.

11 G. Charrada, *et al.*, Synthesis of Sm-Doped CuO–SnO$_2$: FSprayed Thin Film: An Eco-Friendly Dual-Function Solution for the Buffer Layer and an Effective Photocatalyst for Ampicillin Degradation, *Technologies*, 2025, **13**(5), 197.

12 Z.-H. Shi, *et al.*, Synthesis and characterization of an oxygen-controlled CuO/SnO2 sensor for NO2 detection, *Sens. Actuators, B*, 2024, **421**, 136517.

13 A. Mohammed Enad and J. M. Rzaij, Synthesis of CuO Thin Film Incorporated with Nanostructured Nd$_2$O$_3$ Deposited by Pulsed Laser Deposition for Ammonia Sensing Applications, *Nano*, 2025, **20**(03), 2450113.

14 Y. Zhang and X. He, Self-powered photodetector with GeSe/WS$_2$/MoS$_2$ van der Waals heterojunction, *Sens. Actuators, A*, 2025, **381**, 116080.

15 X. Tang, *et al.*, Wafer-Scale Vertical 1D GaN Nanorods/2D MoS$_2$/PEDOT:PSS for Piezophototronic Effect-Enhanced Self-Powered Flexible Photodetectors, *Nano-Micro Lett.*, 2025, **17**(1), 1–15.

16 C. Zhang, *et al.*, Broadband self-powered MoS$_2$/PdSe$_2$/WSe$_2$ PSN heterojunction photodetector for high-performance optical imaging and communication, *Opt. Express*, 2024, **32**(22), 38136–38146.

17 I. Ibrahim, A. Mohammed and A. Ramizy, Responsivity enhancement of lutetium oxide doped-NiO thin films, *J. Ovonic Res.*, 2018, **14**(1), 17–25.

18 A. Mohammed, *et al.*, Nanocrystalline Ce-doped CdO thin films synthesis by spray pyrolysis method for solar cells applications, *J. Ovonic Res.*, 2019, **15**(1), 37–42.

19 S. Keppert, *et al.*, Phase purity and surface morphology of high-Jc superconducting Bi$_2$Sr$_2$Ca$_1$Cu$_2$O$_{8+\delta}$ thin films, *Appl. Surf. Sci.*, 2023, **636**, 157822.

20 S. A. Khalaf, *et al.*, Photoresponse Evaluation of a Multiband Self-Driven SnO2/CuO/Si Heterojunction Photodetector Fabricated by Pulsed Laser Deposition, *ACS Appl. Electron. Mater.*, 2025, **7**(8), 3409–3415.

21 R. Mahlouji, *et al.*, Thickness and Morphology Dependent Electrical Properties of ALD-Synthesized MoS$_2$ FETs, *Adv. Electron. Mater.*, 2022, **8**(3), 2100781.

22 D.-S. Um, *et al.*, High-performance MoS$_2$/CuO nanosheet-on-one-dimensional heterojunction photodetectors, *ACS Appl. Mater. Interfaces*, 2016, **8**(49), 33955–33962.

23 S. Cheung and N. Cheung, Extraction of Schottky diode parameters from forward current-voltage characteristics, *Appl. Phys. Lett.*, 1986, **49**(2), 85–87.

24 E. Y. Salih, Fabrication and photodetection performance evaluation of nanostructured CdS/Si MSM visible light photodetector, *Opt. Mater.*, 2024, **149**, 115120.

25 Y. Lee, *et al.*, Hybrid structures of organic dye and graphene for ultrahigh gain photodetectors, *Carbon*, 2015, **88**, 165–172.

26 A. Ghosh, *et al.*, Staggered band alignment of n-Er$_2$O$_3$/p-Si heterostructure for the fabrication of a high-performance broadband photodetector, *Nano Express*, 2024, **5**(3), 035003.

27 E. T. Salim, *et al.*, Thickness-Engineered Au@Nb$_2$O$_5$ Thin Films for Ultrahigh-Response Photodetectors: Synthesized by Pulsed Laser in Liquid, *Opt. Mater.*, 2025, 117337.

28 E. T. Salim, A. I. Hassan and S. A. Naaes, Effect of gate dielectric thicknesses on MOS photodiode performance and electrical properties, *Mater. Res. Express*, 2019, **6**(8), 086416.

29 Q. Zhao, *et al.*, The role of traps in the photocurrent generation mechanism in thin InSe photodetectors, *Mater. Horiz.*, 2020, **7**(1), 252–262.

30 R. Dutta, *et al.*, Optical enhancement of indirect bandgap 2D transition metal dichalcogenides for multi-functional optoelectronic sensors, *Adv. Mater.*, 2023, **35**(46), 2303272.

31 S. H. Yu, *et al.*, Dye-sensitized MoS$_2$ photodetector with enhanced spectral photoresponse, *ACS Nano*, 2014, **8**(8), 8285–8291.